Article

Surface Investigation of $Ni_{81}Fe_{19}$ Thin Film: Using ARXPS for Thickness Estimation of Oxidation Layers

Zongsheng He [1], Ziyu Li [1], Xiaona Jiang [1], Chuanjian Wu [1], Yu Liu [1], Xinglian Song [2], Zhong Yu [1], Yifan Wang [1](iD), Zhongwen Lan [1] and Ke Sun [1,*]

[1] School of Materials and Energy, University of Electronic Science and Technology of China, Chengdu 610054, China; hezongsheng112@163.com (Z.H.); ziyu.li@uestc.edu.cn (Z.L.); xnjiang@uestc.edu.cn (X.J.); wcjuestc2005@uestc.edu.cn (C.W.); liuyui15005510@163.com (Y.L.); yuzhong@uestc.edu.cn (Z.Y.); complax@163.com (Y.W.); zwlan@uestc.edu.cn (Z.L.)

[2] Shandong Chunguang Magnetoelectricity Technology Co., Ltd., Linyi 276017, China; kongxianjuan@ktong.com

* Correspondence: ksun@uestc.edu.cn; Tel.: +86-028-8320-1637

Abstract: This work demonstrates the dependence between magnetic properties and the thickness of NiFe thin films. More importantly, a quantitative study of the surface composition of NiFe thin film exposed to atmospheric conditions has been carried out employing angle-resolved X-ray photoelectron spectroscopy (ARXPS). In this study, we fabricated $Ni_{81}Fe_{19}$ (NiFe) thin films on Si (100) substrate using electron beam evaporation and investigated their surface morphologies, magnetic properties, and the thickness of the surface oxide layer. The coexistence of metallic and oxidized species on the surface are suggested by the depth profile of ARXPS spectra. The thickness of the oxidized species, including NiO, $Ni(OH)_2$, Fe_2O_3, and Fe_3O_4, are also estimated based on the ARXPS results. This work provides an effective approach to clarify the surface composition, as well as the thickness of the oxide layer of the thin films.

Keywords: permalloy; magnetic thin films; ARXPS; magnetic property; oxidation layer

1. Introduction

Microwave magnetic devices, such as circulators, filters, and phase shifters are indispensable components in satellite and mobile communications systems [1–3]. Recently, the rapid development in the electronic communication industry has proposed higher requirements for microwave devices including higher operating frequency, lower loss, and higher integration level. As magnetoelectronic devices are the core components of microwave devices [4–6], there is an urgent demand to improve their magnetic properties at the high-frequency range. However, most microwave/radio-frequency magnetic components are discrete devices based on bulk materials, and directly reducing the size of high integration often leads to degradation in performance. The progress of chip-type technology is still behind for the perfect integration of magnetic components with existing semiconductor devices. Given the above context, ferromagnetic/anti-ferromagnetic (FM/AF) thin films with a multilayer structure are considered as ideal candidates. The higher saturation magnetization (M_s), permeability (μ), and self-biased ferromagnetic resonance (FMR) frequency of the magnetic thin film make them suitable for high-frequency applications as nanostructured magnetic media and magnetic sensors [7–13]. Meanwhile, the multilayer structure has been widely used in giant magnetoresistance spin valves based on the exchange bias phenomenon.

The operating frequency, FMR linewidth and the resonance field of periodically arranged FM/AF multilayer structure can easily be affected by the change in thickness of each single layer, as well as the surface morphology. Especially, when the thickness of individual layers falls below the critical thickness, the states and properties of surface and

interface dominate the magnetic properties. In the multilayer structure of thin films, the thickness of each single layer can reach down to the level of several nanometers. However, such high accuracy is often susceptible to environmental oxidation, which leads to the change in the effective thickness, as well as the change in composition.

To study the composition of surface and interface as well as the thickness distribution in multilayer structures, atomic force microscopy (AFM) and angle resolved X-ray photoelectron spectroscopy (ARXPS) are commonly applied. Among the previous studies, Yu G.H. et al. [14] studied the relationship between the oxidation states of Ni in NiO_x and the exchange bias field H_{ex} of the NiFe film by ARXPS, but the critical thickness of the pinning of NiFe film was not studied. S.S. Sakhonenkov et al. [15] presented an in-depth study of Mo/Si multilayer systems using ARXPS. They reported that a $MoSi_2$ interlayer with a thickness of 0.19 ± 0.05 nm was identified on the Si-on-Mo interface. J. Zemek et al. [16] investigated the surface and in-depth distribution of sp^2 and sp^3 coordinated carbon atoms in modified diamond-like carbon films. A. Sanchez-Martinez et al. [17] discovered that small amounts of oxidized gallium and metallic arsenic are located at the HfO_2/InGaAs interface. Meanwhile, they studied the structure of TiN/HfO_2 nanofilms grown on InGaAs substrates by ARXPS. The above evidences have shown ARXPS as a useful tool in characterizing the surface/interface of the thin films. In this study, AFM and ARXPS are used to characterize the surface oxidation layers of the NiFe thin film, which is known for its high permeability while having a relatively high M_s. More importantly, the thickness of each oxidation layer is estimated based on the ARXPS results. The static magnetic properties of the NiFe thin films were also investigated.

2. Experimental Details

In this experiment, $Ni_{81}Fe_{19}$ thin films were deposited on 5 mm $\times$ 5 mm Si (100) substrates by electron beam evaporation (EB-500) in vacuum ($\leq 5.0 \times 10^{-5}$ Pa) at 25 °C. The thicknesses of the $Ni_{81}Fe_{19}$ films are 90, 100, 110, and 120 nm. The growth rate of the film is 0.03 nm/s. The Si (100) substrates were preliminarily cleaned in a sequential bath of acetone, alcohol, and deionized water and dried with ionized dry N_2 flux. Once prepared, the samples were stored at room temperature to be oxidized under ambient environment.

The surface morphologies of the NiFe thin films were investigated using an atomic force microscope (AFM, Bruker MultiMode8) with a scanned area of 2 μm $\times$ 2 μm. Static magnetic properties of NiFe films were measured using a vibrating sample magnetometer (VSM, Lake Shore 8604) at room temperature. The samples were analyzed using ARXPS (ULVAC-PHI5000 Veraprobe III) with an Al Kα emission source (1486.6 eV). The XPS measurements were conducted at a base pressure of 8×10^{-10} Pa. The pass energy of the spectrometer was set to 69 eV. The energy was calibrated by setting the adventitious C 1*s* binding energy to 284.8 eV. The chemical depth profile was acquired at six angles (α) of 20°, 35°, 45°, 60°, 75°, and 90°.

3. Results and Discussion

3.1. AFM Analysis and Surface Roughness

Figure 1 illustrates the AFM surface morphology and roughness of the NiFe thin films with a NiFe thicknesses of 100 nm. The surface roughness of the films with different NiFe thicknesses from 90 to 120 nm was 1.31 nm, 1.27 nm, 1.45nm, and 1.67 nm, respectively. The minimum roughness of 1.27 nm is seen for the sample with a thickness of 100 nm, whose average grain size also appears to be the smallest among the samples (see Figure 3a). The experimental results are in good correspondence with a previous report [18], which shows the positive correlation between the average grain size and surface roughness.
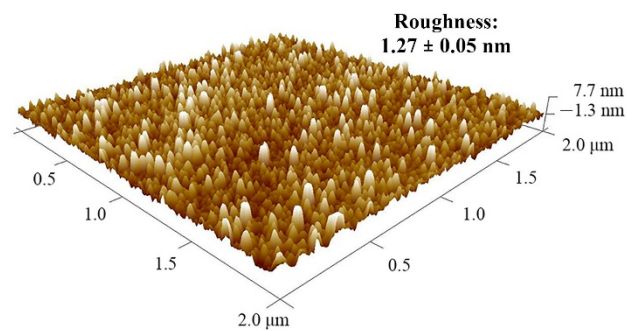
Figure 1. AFM images of NiFe films with a thickness of 100 nm.

3.2. Magnetic Properties of NiFe Films

Figure 2a,b shows the in-plane and out-of-plane magnetic hysteresis loops of NiFe thin films with the thicknesses from 90 to 120 nm. The samples with thickness of 90–110 nm show narrow *M-H* loops, while the 120-nm-thick sample shows a much wider curve, suggesting a higher coercivity (H_c) [19]. Figure 3 shows the static magnetic properties of the NiFe thin films, including the saturation magnetization ($4\pi M_s$) and H_c. According to Figure 3a, as the thickness of NiFe thin film increases, the $4\pi M_s$ is increased. Concomitantly, in-plane ($H_{c//}$) and out-of-plane ($H_{c\perp}$) coercivity are displayed in Figure 3b. Both $H_{c//}$ and $H_{c\perp}$ exhibit a similar trend, which shows a slight reduction upon the increase of thickness from 90 to 110 nm, followed by a dramatic increase as the thickness is further increased to 120 nm. As the H_c is dependent on the quality and defects of the film [20], the dramatic increase of H_c observed in Figure 3b can be attributed to the high roughness of the 120 nm thick sample.

3.3. Oxidation Thickness of NiFe Films

Figure 4 shows the ARXPS spectra of Ni in the NiFe thin film with a thickness of 100 nm from various take-off angles. For clear identification of each peak, as well as to obtain the peak intensity, fitted results for each spectrum are obtained (examples of $\alpha = 20°$ and $90°$ are shown in Figure 5). The relationship between the detection depth (*d*), photoelectron take-off grazing angle, and the mean free path of inelastic scattering (λ), is as follows [21].
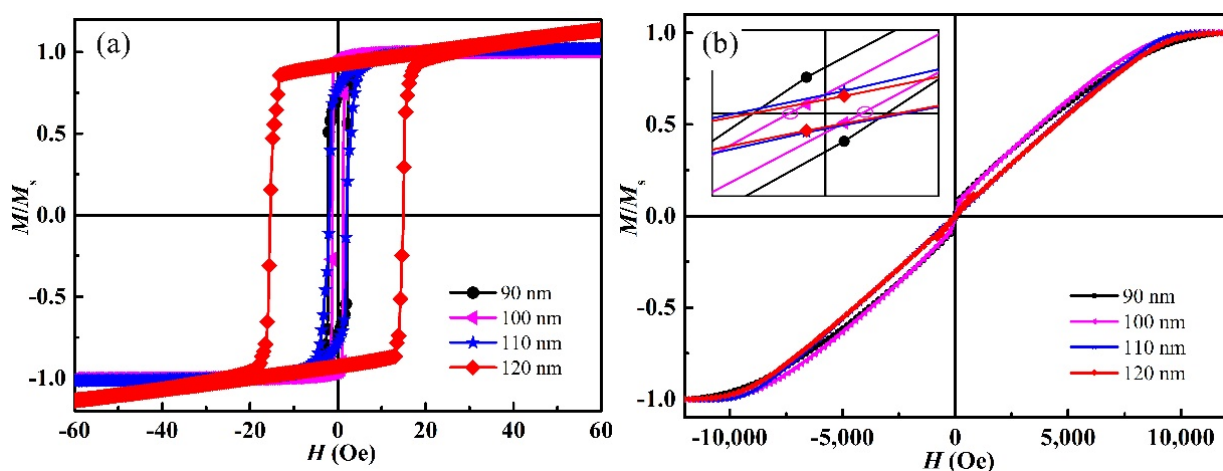
$$d = 3\lambda \sin \alpha \tag{1}$$

Figure 2. The magnetic hysteresis (*M-H*) loops of NiFe thin films with thickness from 90 to 120 nm: (**a**) the in-plane magnetic hysteresis loops, (**b**) the out-of-plane magnetic hysteresis loop.
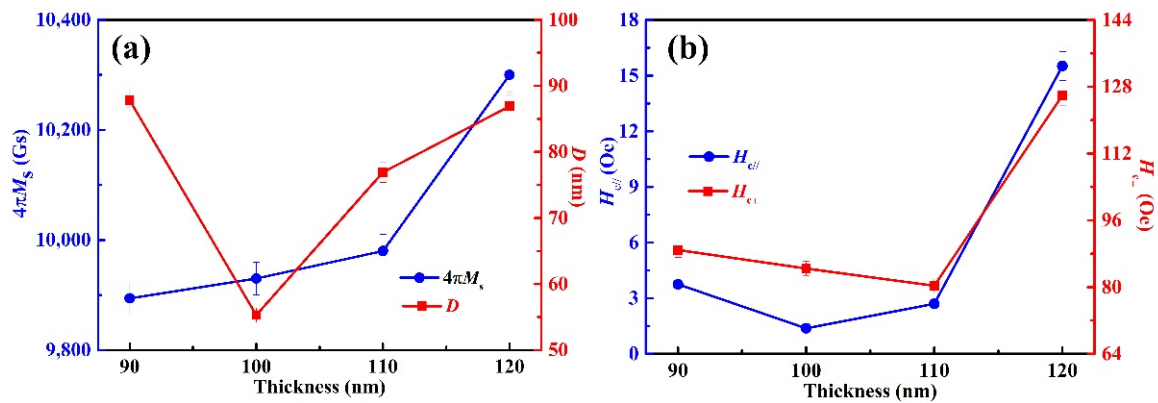
Figure 3. The static magnetic properties of the $Ni_{81}Fe_{19}$ thin films with thicknesses from 90 to 120 nm: (**a**) the saturation magnetization ($4\pi M_s$) and average grain size (D), (**b**) the in-plane ($H_{c//}$) and out-of-plane ($H_{c\perp}$) coercivity.
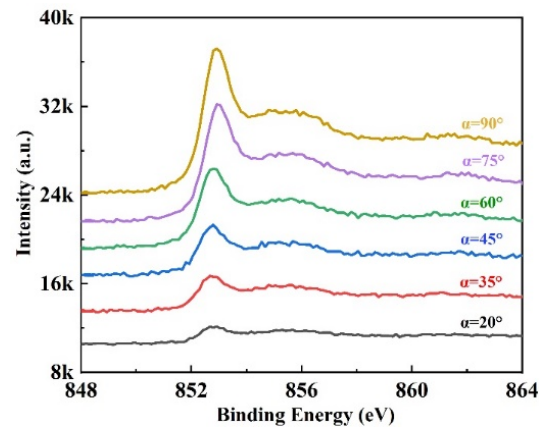

Figure 4. Spectra of Ni 2p photoemission in the NiFe thin film with a thickness of 100 nm at different take-off angles (α).
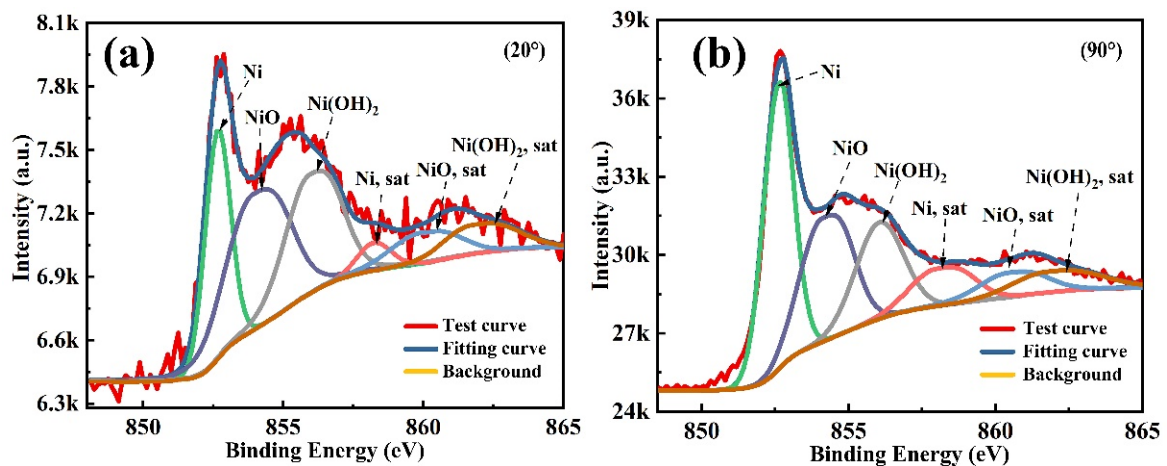
Figure 5. ARXPS spectra of Ni 2p photoemission and the fitting results for NiFe thin film with a thickness of 100 nm at different take-off angles: (**a**) 20° and (**b**) 90°.

As can be seen in Figure 5, there are several noticeable peaks representing the signals from Ni $2p3/2$ (852.3 eV), NiO $2p3/2$ (853.3 eV), $Ni(OH)_2$ $2p3/2$ (856.6 eV), as well as their satellite peaks [22–24]. The coexistence of metallic and oxide components is further confirmed by the spectra from O 1s photoemission, which is shown in Figure 6a. The

thickness of the oxide film (d_o) can be calculated according to the ARXPS results through the following equations [25]:

$$\ln\left(1 + \frac{R}{R_\infty}\right) = \frac{d_o}{\lambda} \cdot \frac{1}{\sin\alpha} \tag{2}$$

where α is different take-off angles: $20°$, $35°$, $45°$, $60°$, $75°$, and $90°$, and R is the ratio of photoelectron peak intensity from the oxides (I_o) to that from nickel (I_s):
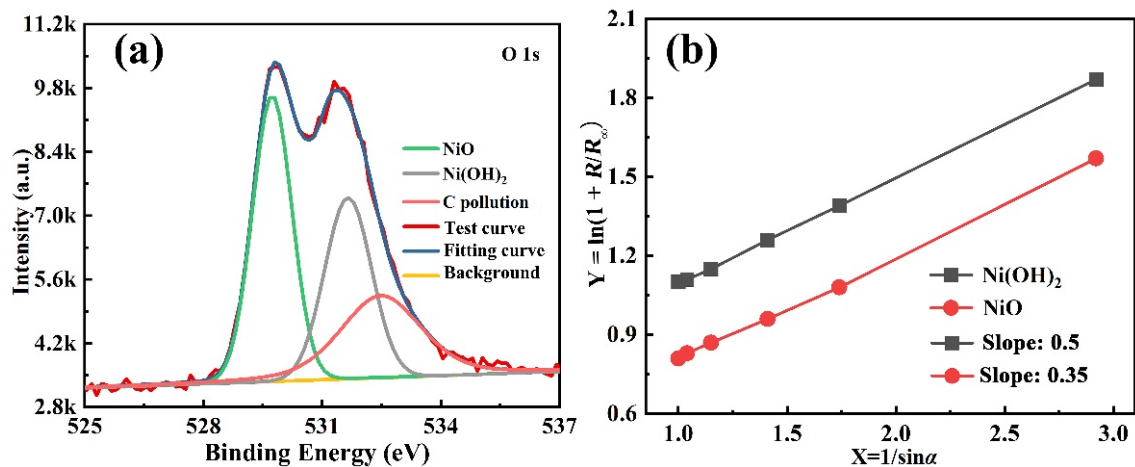
$$R = \frac{I_o}{I_s} \tag{3}$$

Figure 6. (**a**) ARXPS spectra of O 1s photoemission and the fitting results, (**b**) the results of $\ln(1 + R/R_\infty)$ against $1/\sin\alpha$ for the nickel oxides in NiFe thin film.

In Equation (2), R_∞ can be calculated as follows:

$$R_\infty = \frac{M_o}{M_s} \cdot \frac{\rho_s}{\rho_o} \cdot \frac{\lambda_s}{\lambda_o} \tag{4}$$

where the values of M are the molecular weight of nickel oxides (M_o) and nickel (M_s), values of ρ are the density of nickel oxides (ρ_o) and nickel (ρ_s), and values of λ are the mean free path of inelastic scattering for nickel oxides (λ_o) and nickel (λ_s). Because the photoelectron kinetic energy of nickel and its oxides are almost the same, thus λ_o and λ_s are approximately equal [21]. Table 1 shows the values of density, molecular weight for Ni, NiO, and Ni(OH)$_2$, as well as the calculated R_∞ for both nickel oxides.

Table 1. The values of density, molecular weight, and kinetic energy for Ni, NiO, and Ni(OH)$_2$, as well as R_∞ for both nickel oxides.

Material	ρ (g/cm^3)	M (g/mol)	R_∞	Kinetic Energy (eV)
Ni	8.9	59	-	853.3
NiO	6.84	75	0.6	853.6
Ni(OH)$_2$	4.15	93	0.3	855.0

Table 2 shows the relative peak intensities of nickel (I_s) and nickel oxides (I_o) at different take-off angles based on the fitting results shown in Figure 5, as well as the calculated ratios between them (R). As α is increased from 20 to $90°$, I_s(Ni) is seen to increase from ~20 to ~43%, while both I_o(NiO) and I_o(Ni(OH)$_2$) are reduced from ~46 to ~32% and from ~33 to ~26%, respectively. As the oxidation reactions take place at the top surface of the metal substrate, with a limited traveling distance of photoemission signal, it is natural that the detection depth becomes deeper as the take-off angle becomes closer to

90°. Therefore, one can observe the obvious enhancement in I_s(Ni), and slight reduction in I_o(NiO) and I_o(Ni(OH)$_2$).

Table 2. Relative peak intensities (I_s and I_o) and the I_o/I_s ratios for both nickel oxides in the NiFe (100 nm) thin film.

α (°)	I_s(Ni) (%)	I_o(NiO) (%)	I_o(Ni(OH)$_2$) (%)	R(NiO) = I_o(NiO)/I_s	R(Ni(OH)$_2$) = I_o/I_s
20	20.38	46.18	33.44	2.27	1.64
35	32.50	37.95	29.55	1.17	0.91
45	36.73	35.37	27.90	0.96	0.76
60	40.32	33.27	26.41	0.83	0.66
75	42.05	32.29	25.66	0.77	0.61
90	42.57	32.00	25.44	0.75	0.60

According to Equation (2), to calculate the thickness of the oxidation layer, one can plot the results of $\ln(1 + R/R_\infty)$ against $1/\sin\alpha$, the slope of which indicates the thickness divided by the mean free path of inelastic scattering (d_o/λ). Figure 6b shows the results of $\ln(1 + R/R_\infty)$ against $1/\sin\alpha$ for Ni(OH)$_2$ and NiO. Given that λ = 6 Å [26], the thickness of NiO in NiFe thin film is determined to be 0.2 nm, the thickness of Ni(OH)$_2$ is determined to be 0.3 nm.

As with nickel oxides, the composition and thickness of iron oxides can also be determined. Figure 7 shows the Fe 2p photoemission spectra of partially oxidized NiFe thin film. The signals from each take-off angle can be fitted with Fe 2p3/2 (706.8 eV), Fe$_2$O$_3$ 2p3/2 (710.7 eV), and Fe$_3$O$_4$ 2p3/2 (709.3 eV) [27–29], the results of which are shown in Figure 8. Figure 9a shows the fitted O 1s spectra to further confirm the existence of iron oxides. Table 3 shows the relevant parameters including I_s(Fe), I_o(Fe$_2$O$_3$), I_o(Fe$_3$O$_4$), and the intensity ratios between iron and its oxides. For the same reason mentioned above, I_s(Fe) is increased with increasing α, as higher take-off angle results in deeper detection depth.
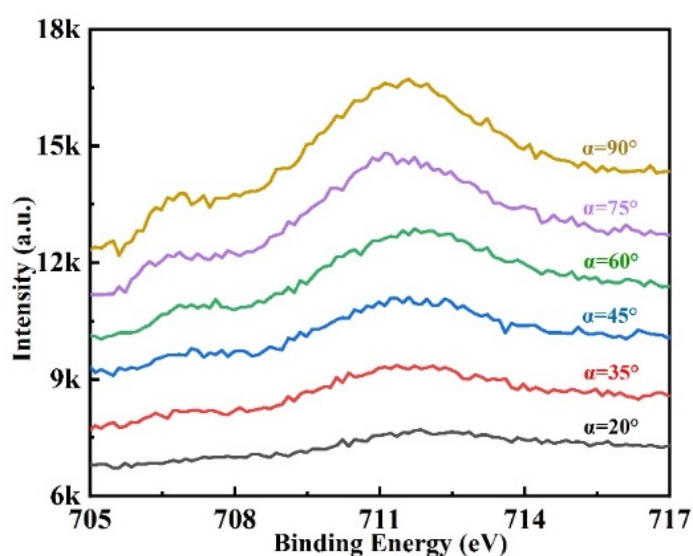

Figure 7. Spectra at different take-off angle of Fe 2p in NiFe(100 nm) thin film.
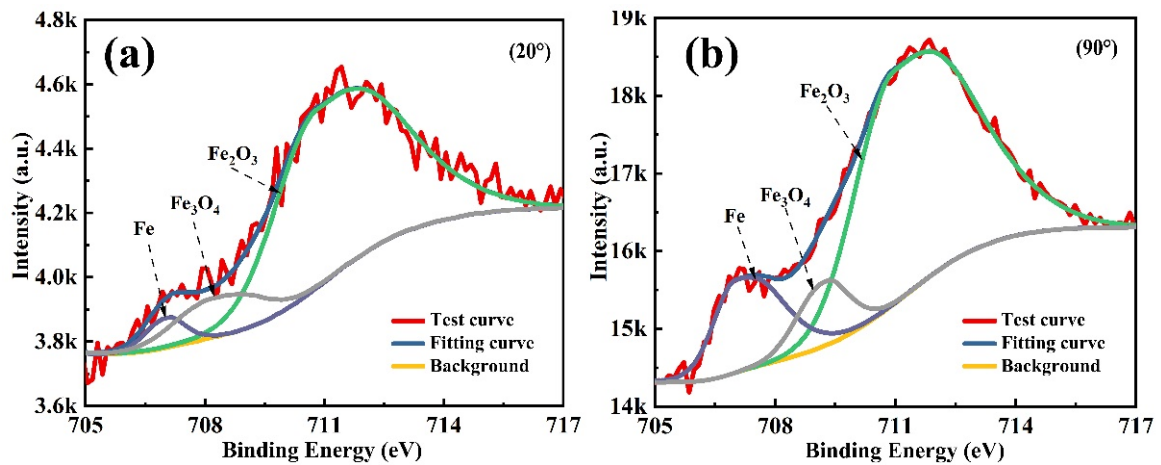
Figure 8. ARXPS spectra of Fe 2p photoemission and the peak fitting results for NiFe thin film with a thickness of 100 nm at different take-off angles of: (**a**) 20° and (**b**) 90°.
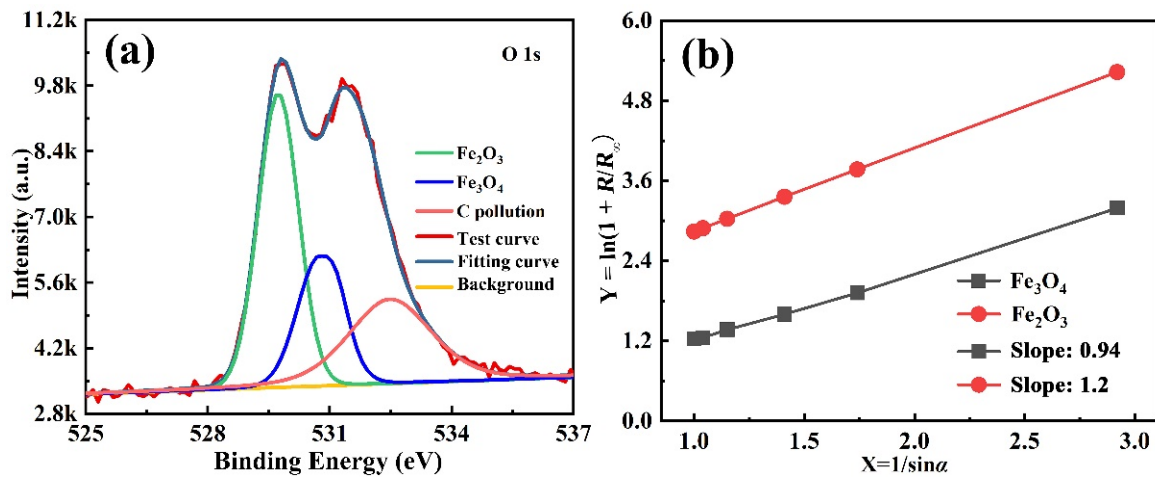

Figure 9. (**a**) ARXPS spectra of O 1s photoemission and the fitting results, (**b**) the results of $\ln(1 + R/R\infty)$ against $1/\sin\alpha$ for the iron oxides in NiFe thin film.

Table 3. Relative peak intensities (I_s and I_o) and the I_o/I_s ratios for both iron oxides in the NiFe (100 nm) thin film.

α (°)	I_s(Fe) (%)	I_o(Fe$_3$O$_4$) (%)	I_o(Fe$_2$O$_3$) (%)	R(Fe$_3$O$_4$) = I_o(Fe$_3$O$_4$)/I_s	R(Fe$_2$O$_3$) = I_o(Fe$_2$O$_3$)/I_s
20	2.11	7.85	90.04	3.72	42.67
35	8.59	8.01	83.41	0.93	9.71
45	12.49	7.92	79.58	0.63	6.37
60	16.63	7.75	75.61	0.47	4.55
75	18.91	7.63	73.46	0.40	3.88
90	19.63	7.59	72.78	0.39	3.71

Table 4 shows the values of density, molecular weight for Fe, Fe$_3$O$_4$, and Fe$_2$O$_3$, as well as the calculated R$_\infty$ for both iron oxides. The values in Tables 3 and 4 are integrated into Equations (2)–(4), and the results of $\ln(1 + R/R_\infty)$ against $1/\sin\alpha$ for Fe 2p photoemission in the NiFe thin film are shown in Figure 9b. As λ = 7.5 Å [26], the thickness of Fe$_2$O$_3$ layer determined is 0.9 nm and that of Fe$_3$O$_4$ is 0.7 nm. It means that oxidation in the natural environment occurs only in the extreme depth of the surface. To summarize, a schematic illustration is shown in Figure 10 to better demonstrate the multilayer structure of the oxidized NiFe.

Table 4. The values of density, molecular weight, and kinetic energy for Fe, Fe_2O_3, and Fe_3O_4, as well as R_∞ for both iron oxides.

Material	ρ (g/cm^3)	M (g/mol)	R_∞	Kinetic Energy (eV)
Fe	7.86	56	-	710.7
Fe_2O_3	5.24	160	0.23	710.4
Fe_3O_4	5.18	232	0.16	710.8
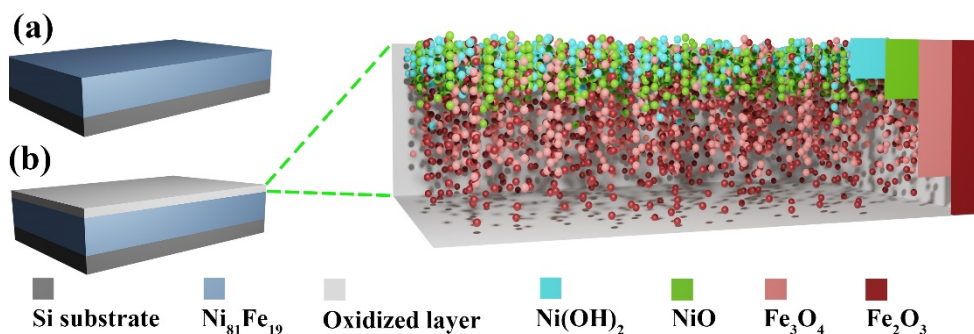
Figure 10. The schematic diagram of NiFe thin film: (**a**) unoxidized, (**b**) oxidized.

4. Conclusions

In summary, NiFe thin films with thickness from 90 to 120 nm were fabricated by electron beam evaporation. The sample with a thickness of 100 nm shows the lowest surface roughness and the smallest grain size. The saturation magnetization of the films is increased from 9891 to 10,300 Gs as the thickness of film increases. The optimum magnetic properties ($4\pi M_s$ = 9930 Gs, H_c = 1.37 Oe) are obtained when the thickness of film is 100 nm. In addition, the coexistence of NiFe and its oxides on the top surface is observed along the probing depth of ARXPS. By fitting the ARXPS spectra and obtaining the relative intensity of each peak, the thickness of NiO, Ni(OH)$_2$, Fe_2O_3, and Fe_3O_4, which are 0.3 nm, 0.2 nm, 0.9 nm, and 0.7 nm, respectively, are determined. This work demonstrates the beneficial application of ARXPS in characterizing the oxide layers including their compositions and thicknesses as a quick and damage-free approach, especially for future investigations with even lower film thickness.

Author Contributions: Conceptualization, K.S.; funding acquisition, K.S.; investigation, Z.H., X.S. and X.J.; methodology, Z.H.; software, Y.L. and Y.W.; supervision, C.W., Z.Y., Z.L. (Zhongwen Lan) and K.S.; writing—original draft, Z.H.; writing—review and editing, Z.H. and Z.L. (Ziyu Li). All authors have read and agreed to the published version of the manuscript.

Institutional Review Board Statement: Not applicable.

Informed Consent Statement: Not applicable.

Data Availability Statement: Not applicable.

Conflicts of Interest: The authors declare that they have no known competing financial interests or personal relationships that could have appeared to influence the work reported in this paper.

References

1. Su, Z.; Bennett, S.; Hu, B.; Chen, Y.; Harris, V.G. Magnetic and microwave properties of U-type hexaferrite films with high remanence and low ferromagnetic resonance linewidth. *J. Appl. Phys.* **2014**, *115*, 17A504. [CrossRef]
2. Belyaev, B.A.; Lemberg, K.V.; Serzhantov, A.M.; Leksikov, A.A.; Bal'va, Y.F. Magnetically tunable resonant phase shifters for UHF band. *IEEE Trans. Magn.* **2015**, *51*, 1–5. [CrossRef]
3. Sharma, V.; Khivintsev, Y.; Harward, I.; Kuanr, B.K.; Celinski, Z. Fabrication and characterization of microwave phase shifter in microstrip geometry with Fe film as the frequency tuning element. *J. Magn. Magn. Mater.* **2019**, *489*, 165412. [CrossRef]

4. Kuanr, B.K.; Veerakumar, V.; Camley, R.E.; Celinski, Z. Permalloy (NiFe) nanometer square-antidot arrays: Dynamic modes and use as a monolithic microwave band-pass filter. *J. Magn. Magn. Mater.* **2019**, *484*, 272–278. [CrossRef]

5. Lu, Q.; Yu, B.; Hu, Z.; He, Y.; Hu, T.; Zhao, Y.; Wang, Z.; Zhou, Z.; Cui, W.; Liu, M. Surface roughness evolution induced low secondary electron yield in carbon coated Ag/Al substrates for space microwave devices. *Appl. Surf. Sci.* **2020**, *501*, 144236. [CrossRef]

6. Paiva, D.V.M.; Silva, M.A.S.; Sombra, A.S.B.; Fechine, P.B.A. Properties of the Sr_3MoO_6 electroceramic for RF/microwave devices. *J. Alloys Compd.* **2018**, *748*, 766–773. [CrossRef]

7. Chen, Y.; Fan, X.; Zhou, Y.; Xie, Y.; Wu, J.; Wang, T.; Chui, S.T.; Xiao, J.Q. Designing and tuning magnetic resonance with exchange interaction. *Adv. Mater.* **2015**, *27*, 1351–1355. [CrossRef]

8. Belmeguenai, M.; Martin, T.; Woltersdorf, G.; Bayreuther, G.; Baltz, V. Microwave spectroscopy with vector network analyzer for interlayer exchange-coupled symmetrical and asymmetrical NiFe/Ru/NiFe. *J. Phys. Condens. Matter.* **2008**, *20*, 345206. [CrossRef]

9. Li, S.; Li, Q.; Xu, J.; Yan, S.; Miao, G.X.; Kang, S.; Dai, Y. Tunable optical mode ferromagnetic resonance in FeCoB/Ru/FeCoB synthetic antiferromagnetic trilayers under uniaxial magnetic anisotropy. *Adv. Funct. Mater.* **2016**, *26*, 3738–3744. [CrossRef]

10. Xu, F.; Liao, Z.; Huang, Q.; Phuoc, N.N.; Ong, C.K.; Li, S. Influence of thickness on magnetic properties and microwave characteristics of NiFe/IrMn/NiFe Trilayers. *IEEE Trans. Magn.* **2011**, *47*, 3486–3489. [CrossRef]

11. Naik, R.; Kota, C.; Payson, J.S.; Dunifer, G.L. Ferromagnetic-resonance studies of epitaxial Ni, Co, and Fe films grown on Cu(100)/Si(100). *Phys. Rev. B* **1993**, *48*, 1008–1013. [CrossRef]

12. Chappert, C.; Le Dang, K.; Beauvillain, P.; Hurdequint, H.; Renard, D. Ferromagnetic resonance studies of very thin cobalt films on a gold substrate. *Phys. Rev. B* **1986**, *34*, 3192–3197. [CrossRef]

13. Biondo, A.; Nascimento, V.P.; Lassri, H.; Passamani, E.C.; Morales, M.A.; Mello, A. Structural and magnetic properties of $Ni_{81}Fe_{19}$/Zr multilayers. *J. Magn. Magn. Mater.* **2004**, *277*, 144–152. [CrossRef]

14. Yu, G.; Zhao, H.; Teng, J.; Chai, C.; Zhu, F.; Xia, Y.; Chai, X. XPS Studies of magnetic multilayers. *J. Univ. Sci. Technol. B* **2001**, *8*, 210–213.

15. Sakhonenkov, S.S.; Filatova, E.O.; Gaisin, A.U.; Kasatikov, S.A.; Konashuk, A.S. Angle resolved photoelectron spectroscopy as applied to X-ray mirrors: An in-depth study of Mo/Si multilayer systems. *Phys. Chem. Chem. Phys.* **2019**, *21*, 25002–250109. [CrossRef]

16. Zemek, J.; Houdkova, J.; Jiricek, P.; Jelinek, M. Surface and in-depth distribution of sp^2 and sp^3 coordinated carbon atoms in diamond-like carbon films modified by argon ion beam bombardment during growth. *Carbon* **2018**, *134*, 71–79. [CrossRef]

17. Sanchez-Martinez, A.; Ceballos-Sanchez, O.; Vazquez-Lepe, M.O.; Duong, T.; Arroyave, R. Diffusion of In and Ga in TiN/HfO_2/InGaAs nanofilms. *J. Appl. Phys.* **2013**, *114*, 143504. [CrossRef]

18. Dong, B.Z.; Fang, G.J.; Wang, J.F.; Guan, W.J.; Zhao, X.Z. Effect of thickness on structural, electrical, and optical properties of ZnO: Al films deposited by pulsed laser deposition. *J. Appl. Phys.* **2007**, *101*, 033713. [CrossRef]

19. Akhter, M.A.; Mapps, D.J.; Ma Tan, Y.Q.; Petford-Long, A.; Doole, R. Thickness and grain-size dependence of the coercivity in permalloy thin films. *J. Appl. Phys.* **1997**, *81*, 4122–4124. [CrossRef]

20. Berzins, A.; Smits, J.; Petruhins, A. Characterization of Microscopic ferromagnetic defects in thin films using magnetic microscope based on nitrogen-vacancy centres. *Mater. Chem. Phys.* **2021**, *267*, 124617. [CrossRef]

21. John, F.W.; John, W. *An Introduction to Surface Analysis by XPS and AES*, 1st ed.; East China University of Technology Publisher: Shanghai, China, 2008.

22. Nagarkar, P.V.; Kulkarni, S.K.; Umbach, E. Surface oxidation investigation of $Ni_{36}Fe_{32}Cr_{14}P_{12}B_6$ glass using angle resolved XPS. *Appl. Surf. Sci.* **1987**, *29*, 194–222. [CrossRef]

23. Biesinger, M.C.; Payne, B.P.; Grosvenor, A.P.; Lau, L.W.M.; Gerson, A.R.; Smart, R.S.C. Resolving surface chemical states in XPS analysis of first row transition metals, oxides and hydroxides: Cr, Mn, Fe, Co and Ni. *Appl. Surf. Sci.* **2011**, *257*, 2717–2730. [CrossRef]

24. Dupin, J.C.; Gonbeau, D.; Vinatier, P.; Levasseur, A. Systematic XPS studies of metal oxides, hydroxides and peroxides. *Phys. Chem. Chem. Phys.* **2000**, *2*, 1319–1324. [CrossRef]

25. Wang, J.Q. *Introduction to Electron Spectroscopy (XPS/XAES/UPS)*; National Defense Industry Publisher: Beijing, China, 1992.

26. Cao, Q.X.; Lei, T.M.; Huang, Y.X.; Li, G.F. *Fundamentals of Solid Physics*; Xidian University Publisher: Xi'an, China, 2008.

27. Yamashita, T.; Hayes, P. Analysis of XPS spectra of Fe^{2+} and Fe^{3+} ions in oxide materials. *Appl. Surf. Sci.* **2008**, *254*, 2441–2449. [CrossRef]

28. Grosvenor, A.P.; Kobe, B.A.; Biesinger, M.C.; McIntyre, N.S. Investigation of multiplet splitting of Fe 2p XPS spectra and bonding in iron compounds. *Surf. Interface Anal.* **2004**, *36*, 1564–1574. [CrossRef]

29. Carver, J.C.; Schweitzer, G.K.; Carlson, T.A. Use of X-ray photoelectron spectroscopy to study bonding in Cr, Mn, Fe, and Co compounds. *J. Chem. Phys.* **1972**, *57*, 973–982. [CrossRef]